Near-field Nanoscopy of Thermal Evanescent Waves on Metals

S. Komiyama,[1*] Y. Kajihara,[1,2] K. Kosaka[1], T. Ueda[1], and Zhenghua An[3]

[1] Department of Basic Science, The University of Tokyo, Komaba 3-8-1, Meguro-ku, Tokyo, 153-8902, Japan.
[2] Institute of Industrial Science, The University of Tokyo, Komaba 4-6-1, Meguro-ku, Tokyo, 153-8505, Japan.
[3] State Key Laboratory of Surface Physics, Department of Physics, and Collaborative Innovation Center of Advanced Microstructures, Fudan University, Shanghai 200433, PR China
 *e-mail: csusukom@mail.ecc.u-tokyo.ac.jp

Intense electromagnetic evanescent fields are thermally excited in near fields on material surfaces (at distances smaller than the wavelength of peak thermal radiation). The property of the fields is of strong interest for it is material-specific and is important for understanding a variety of surface-related effects, such as friction forces, Casimir forces, near-field heat transfer, and surface-coupled molecular dynamics. On metal surfaces, relevance of surface plasmon polaritons (SPlPs), coupled to collective motion of conduction electrons, has attracted strong interest, but has not been explicitly clarified up to the present time. Here, using a passive terahertz (THz) near-field microscope with unprecedented high sensitivity, we unveil detailed nature of thermally generated evanescent fields (wavelength: $\lambda_0 \approx 14.5 \mu m$) on metals at room temperature. Our experimental results unambiguously indicate that the thermal waves are short-wavelength fluctuating electromagnetic fields, from which relevance of SPlPs is ruled out.

Existence of intense thermal electromagnetic evanescent fields[1] on metals and polar dielectrics has been experimentally proved by a series of measurements, in which radiative heat conduction between two bodies dramatically increases in the near field.[2-8] In the case of polar dielectrics, it is established that the evanescent fields are dominated by surface phonon polaritons (SPhPs), which yields quasi monochromatic sharp peak in the spectrum.[5-8] By analogy to the SPhP in dielectrics, one would expect that surface plasmon polaritons (SPlPs)[9-11] play a key role in metals. About a decade ago de-Wilde et al. reported observation of thermally excited SPlPs based on the fringe-like interference patterns seen in the images of passive scattering–type scanning near-field optical microscope (s-SNOM) on heated Au layers.[12] Our work is a thorough reexamination of thermal electromagnetic evanescent fields on metals with an improved passive s-SNOM ($\lambda_0 = 14.5 \pm 0.7$ μm). Owing to ultra-high sensitivity and unprecedented high spatial resolution (20 nm), our measurements unveil detailed new features of the waves that are largely different from those reported by de-Wilde et al.[12]: Thermal evanescent fields are utterly dominated by fluctuating electromagnetic fields with extremely short in-plane wave lengths $\lambda_{//} \ll \lambda_0$ and extremely short out-of-plane decay lengths $l_z \ll \lambda_0$, which do not exhibit discernible interference pattern in the near-field image: Relevance of SPlPs in the infrared spectral region is thereby ruled out. All of the experimental findings, including temperature dependence, are consistently explained by existing theories,[1,13,14] and establish deeper understanding of thermally excited electromagnetic waves on metals.

Experimental challenge in the study of thermal evanescent waves on metals at not too high temperatures stems from the fact that thermal energy density spectrum in the near field is monotonous without a characteristic peaked structure.[1] This is different from polar dielectrics, in which sharp radiation spectrum of SPhPs can be exploited as a distinct signature for identifying thermal evanescent waves.[1,15] For characterizing the waves on metals, therefore, frequency spectroscopy is inadequate and the study of wave vectors $\boldsymbol{k} = (\boldsymbol{k}_{//}, k_\perp)$ relevant to the waves at a given frequency is essential, where the wave vector, $\boldsymbol{k}_{//}$, parallel to the surface corresponds to the inverse in-plane wavelength, $\lambda_{//} = 2\pi/k_{//}$ with $k_{//} = |\boldsymbol{k}_{//}|$ and the wave number, $k_\perp$, in the direction normal to the surface, being imaginary, implies the inverse out-of-plane decay length, $l_z = 1/ik_\perp$ of the wave. Here $k_{//}$ for evanescent waves is larger than the wave number $k_0 = 2\pi/\lambda_0 = \omega/c$ in vacuum (ω; the angular frequency, c; the light velocity in vacuum) because $k_{//}^2 + k_\perp^2 = k_0^2$ is satisfied. To have experimental access to $\boldsymbol{k}$, we have developed an ultra-highly-sensitive passive scattering-type scanning near-field optical microscope (s-SNOM) in the long-wavelength infrared (LWIR) region (Fig. 1). With the improved s-SNOM system, quasi-quantitative analysis of the wave vectors involved in the waves was made possible in a reliable method, and deeper understanding of thermal evanescent waves on metals has been achieved.

Results

Sensitive passive s-SNOM and extraction of near-field signals. Special attention should be paid in the high-resolution passive s-SNOM measurements of metals, in which thermal evanescent waves, generated without external illumination, is scattered by a sharp probe tip to be detected. The first point to be noted is that the relevant energy flux of the tip-scattered near-field thermal radiation is so small as to be not readily detectable by commercially available detectors. In polar dielectrics the energy density of thermal evanescent waves is sharply peaked at the resonant peak of SPhP, but such enhancement structure is absent in metals. In several measurements, samples are heated up for intensifying the signal, but heating up the sample causes serious complication in measurements as described later. In order to obtain near-field signals without heating up samples, we apply an ultra-highly sensitive LWIR detector, called CSIP,[16] and incorporate it in a specially designed home-made LWIR confocal microscope (see Methods).[17]

The second point to be noted is that the signal of small energy flux lies buried in much stronger far-field background radiation, which primarily arises from the spontaneous emission and the reflection of ambient radiation, both from the sample surface in the focus spot of the confocal microscope. The near-field signal component is maximized in our measurement system, but still, it is only a fraction about $10^{-3} \sim 10^{-4}$ of the far-field background component. This is a serious issue for the study of metals because the spectrum of near-field evanescent radiation cannot be readily distinguished from that of the far-field background radiation. It is, therefore, essential to extract the near-field component in a reliable method, and to make sure that the near-field signal component is correctly extracted by carefully examining the consistency of obtained results. For this sake, we oscillate the probe tip height independently of the control of the atomic force microscope (AFM) (see Methods).[18] The probe tip height moves between the bottom position, h, and the top-most position, $h+\Delta h$, where the values of h and Δh are arbitrarily chosen in each measurement ($h =10 \sim$ 400 nm, $\Delta h = 0 \sim 200$ nm). Letting $I(h)$ and $I(h+\Delta h)$ be the detector signals when the tip position is at h and $h+\Delta h$, we study the fundamental demodulated signal, $I_f(h) = I(h) - I(h+\Delta h)$, or the second-order demodulation signal, $I_{2f}(h) = I_f(h) - I_f(h+\Delta h)$ (see Methods). In our measurements the non-modulated detector signal $I(h)$ practically represents the far-field signal since $I_f(h)$, $I_{2f}(h) <<$ $I(h)$.

In active measurements of s-SNOM, which utilizes external illumination,[19-23] it is widely known that far-field component is not filtered out in the fundamental demodulation signal, $I_f(h)$. This is because a bulky probe shaft high above the tip scatters incident radiation, causing a significant portion of un-filtered far-field components in $I_f(h)$. This effect is indicated by a long artificial tail of $I_f(h)$ extending to larger values of h. Accordingly, active s-SNOM measurements adopt second-order demodulation signal, $I_{2f}(h)$, or still-higher order demodulation signals.[20-23] We expect that, in passive measurements as well, if the sample is heated up, the sample works as an intensified radiation source, the spontaneous emission from which is scattered by the probe shaft and causes a significant un-filtered far-field component in $I_f(h)$. To avoid such complication of measurements, we place our

samples at ambient temperature. Later we will mention different situation in the work of de Wilde et al.[12]

Near-field signals. Our study includes measurements on numerous samples of patterned layers of several metals (Au, Al, and Ti) deposited on different substrates (GaAs, SiC, and SiO2). (See Methods). In this report we focus fundamental features of metals, which are found to be similar among different metals. Figures 2a shows a sample of Au layer patterned on a GaAs substrate. In the image of far-field signal I without probe modulation (Fig. 2b), concentric Au rings are not resolved because the resolution $\Delta X_{FF} \approx 15$ μm is not sufficient. By modulating the probe ($h = 10$ nm, $\Delta h = 100$ nm), the detailed structure is clearly visualized in the image of near-field signal I_f (Fig. 2c).

Figures 2d-f displays another series of measurements on a relatively large Au disk on a SO2 substrate. Near-field image (I_f) is shown in Fig. 2d. The near-field signal (I_f) and the far-field signal (I) recorded in a line scan are compared in Fig. 2e. The two signals are noted to exhibit opposite contrast between Au and SiO2; viz., SiO2 is brighter in the far field, but Au is brighter in the near field: We note that the same is true also for the contrast between Au and GaAs in Fig. 2b. In far fields, SiO2 and GaAs are brighter. This is because the emissivities are higher than that of Au. The near field radiation on SiO2 or GaAs, however, is weak because the resonant SPhP frequency in each material is away from the frequency in study ($\omega = 1.30 \times 10^{14}$ rad/s).

At the boundaries of Au/GaAs and Au/SiO2 (Figs. 2 c and e), the edge resolution is noted to be $\Delta X_{NF} \approx 60$ nm $\approx 0.004\ \lambda_0$. The radius of curvature of the tip apex of the probe used is found to be $R \approx 50$ nm in a SEM image. Additional experiments using different probe tips ($R = 200 \sim 20$ nm) show that the resolution is roughly determined by R : Particularly, $\Delta X_N \approx 20$ nm is achieved with the sharpest probe tip with $R \approx 20$ nm. To examine how far the near-field radiation extends out of the surface, we study I_f ($\Delta h = 25$ nm) as a function of h on the Au disk shown in Fig. 2d. Figure 2f shows that I_f rapidly decreases as h increases, yielding a characteristic decay length of $L_z \approx 40$ nm $\sim 0.003\ \lambda_0$. We also studied I_{2f} and found a similar decay profile ($L_z \approx 30$ nm). We studied the decay profile of I_f and I_{2f} on a number of other metal samples (Au, Al and Ti) of different shapes, and confirmed similar decay lengths: The signals practically vanish at $h \approx 150$ nm in all the samples studied. These results indicate unambiguously that the electromagnetic evanescent fields are strictly confined in the close vicinity of the surface in a range $h < 150\sim200$ nm.

In order to estimate absolute energy density of the evanescent waves, we return to Fig. 2e and note that $I_f(h,\ \Delta h) = I(h) - I(h + \Delta h) = 440$ pA while $I(h) = 261$ nA on Au ($h = 10$ nm, $\Delta h = 100$ nm). Noting the decay profile of Fig. 2f and also considering that the near-field and the far-field components originate from the areas respectively given by ΔX_{NF}^2 and ΔX_{FF}^2, the respective energy fluxes emitted from unit area are, respectively, $I_f/(\Delta X_{NF})^2$ and $I/(\Delta X_{FF})^2$, from which $\{I_f/(\Delta X_{NF})^2\}/\{I/(\Delta X_{FF})^2\} \approx 100$ is obtained with $\Delta X_{NF} \approx 20\sim60$ nm and $\Delta X_{FF} \approx 15$ μm. Noting that the efficiency of the evanescent waves being scattered by the tip and being guided to the detector is

substantially less than unity and that finite emissivity of optical components also contribute to I, we can conclude that the energy density of the near-field radiation (at $h = 10$ nm) is higher than that of the black-body by a factor larger than 100. The decay profile and the energy density of the evanescent waves are also studied on Al and Ti, and similar results are obtained.

We note that the near-field image of the Au disk in Fg. 2d is structure-less, without exhibiting any interference patterns ascribable to SPlP-mode waves. (Considering the disk diameter and the wavelength of SPlP waves, six to seven concentric fringes should be visible in the disk if SPlPs are present.) By examining other numerous metal patterns of different size and shape, we are convinced that no interference pattern ascribable to SPlPs is visible. This is different from the earlier report of de Wilde et al.[12], as will be discussed later.

Two characteristic lengths, $\Delta X_{NF} \sim 20$ nm and $L_z \sim 40$ nm, of the evanescent waves strongly suggest, without invoking particular interpretation, that the evanescent electromagnetic fields ($h = 10$ nm) on metals are dominated by those of short in-plane wavelengths $\lambda_{//} < 2\pi \Delta X_{NF} \sim 0.01 \lambda_0$ and short decay lengths $L_z \sim 40$ nm $\sim 0.003 \lambda_0$; in terms of wave numbers, $k_{//} > 100 k_0$ and $ik_\perp \sim 50 k_0$. These features of the waves are consistent with the absence of the signature of SPlP-mode waves because the SPlP-mode in the long wave infrared range ($\omega << \omega_{SPR}$) is characterized by $k_{//} \approx k_0$ and $ik_\perp \sim 0 << k_0$ (or $\lambda_{//} \approx \lambda_0$, $L_z >> \lambda_0$).

In order to crucially test our interpretation, we study a series of metal disks with systematically varying the disk diameter D from 16 μm down to 0.4 μm. The idea behind this test is straightforward: The near-field radiation intensity on a disk of D will be reduced with decreasing D because generation of those evanescent waves with in-plane wavelengths, $\lambda_{//}$, exceeding D will be suppressed. The study is made for Au and Al disks. As shown in the inset of Fig. 3, each metal disk is separated from the substrate metal by a 100-nm-thick Al_2O_3 spacer layer. Figure 3 shows that the intensity of I_f is kept nearly unchanged with decreasing D down to $D_c \sim 1$ μm $\sim 0.07 \lambda_0$ but starts decreasing rapidly below D_c. This feature makes certain that the evanescent waves are dominated by those of short in-plane wavelengths, $\lambda_{//} < D_c \sim 1$ μm $\sim 0.07 \lambda_0$ or large wave numbers $k_{//} > 14 k_0$, and again, rules out possible relevance of SPlP waves.

Though not shown here, we have studied temperature dependence of I_f on Au, Al, and Ti in a rage of 10 °C $< T <$ 60 °C and confirmed that the signal increases with increasing T, following a relation consistent with $I_f \propto 1/\{\exp(\hbar\omega/k_B T) - 1\}$ ($\hbar$; the Dirac constant, k_B; the Boltzmann constant). This shows that the evanescent waves in study are thermally excited.

Comparison with theory

Electromagnetic local density of states (LDOS). All of our experimental findings described in the above are consistently accounted for by existing theories. The density of electromagnetic energy of thermally exited radiation (angular frequency ω) at distance z from the surface of a semi-infinite material at temperature T,

$$U(z,\omega) = \rho(z,\omega)\,[\hbar\omega\,/\,\{\exp(\hbar\omega/k_B T)-1\}], \qquad (1)$$

has been theoretically derived, [1,13,14,24] where $\rho(z,\omega)$, called the electromagnetic local density of states (LDOS), is given by

$$\rho(z,\omega) = \rho_{PG} + \rho_{EV} = (\rho_0/2)\{\int_0^1 P_{PG}(K_{//}, z,\omega)\,\mathrm{d}\,K_{//} + \int_1^\infty P_{EV}(K_{//}, z,\omega)\,\mathrm{d}\,K_{//}\}, \qquad (2)$$

with $\rho_0 = \omega^2/(\pi^2 c^3)$ being the LDOS in vacuum. Here ρ_{PG} and ρ_{EV} are the contributions from propagating and evanescent wave components, respectively, which are obtained by integrating

$$P_{PG}(K_{//}, z,\omega) = (K_{//}/K_\perp)\{2 + K_{//}^2[\mathrm{Re}(r_{12}^s e^{2i\,K_\perp \omega z/c}) + \mathrm{Re}(r_{12}^p e^{2iK_\perp \omega z/c})]\} \qquad (3)$$

and

$$P_{EV}(K_{//}, z,\omega) = (K_{//}^3/|K_\perp|)[\mathrm{Im}(r_{12}^s) + \mathrm{Im}(r_{12}^p)]e^{-2|K_\perp|\omega z/c)]} \qquad (4)$$

in respective intervals of $K_{//}$. Here, $\boldsymbol{K}= (\boldsymbol{K}_{//}, K_\perp) = \boldsymbol{k}/k_0 = (\boldsymbol{k}_{//}, k_\perp)/k_0$ with $K_{//} = |\boldsymbol{K}_{//}|$ are the normalized wave vector satisfying $K_{//}^2 + K_\perp^2 = 1$, where $K_\perp$ is real for propagating waves ($0 < K_{//} < 1$) and imaginary for evanescent waves ($1 < K_{//}$). r_{12}^s and r_{12}^p are the Fresnel reflection coefficients for s- and p-polarizations determined by the complex dielectric constant $\varepsilon(\omega)$ of metals, which we approximate with the Drude model.[25] While each LDOS consists of the contributions from electric and magnetic components,[1,13,14] we discuss the total LDOS here.

Figure 4a displays results of calculation for Au at $\omega=1.30 \times 10^{14}$/s. The LDOS, $\rho = \rho_{PG} + \rho_{EV}$, takes large values by more than four orders of magnitude higher than ρ_0 (black-body) at $z \approx 10$ nm, but rapidly decreases to a value close to ρ_0 at $z \approx 400$ nm, above which ρ is nearly a constant at $\rho \approx \rho_0$. The contribution from propagating-waves, ρ_{PG}, is negligibly small in the near-field domain ($z < 200$ nm). The nature of the intense evanescent waves is elucidated in Fig. 4b, where two groups are distinguished. One is a group of SPlP-mode p-polarized surface waves, which are given by the pole of r_{12}^p in Eq.(4) and form an extremely sharp peak at $K_{//} = [\varepsilon/(\varepsilon+1)]^{1/2} \approx 1.000045$ ($iK_\perp \ll 1$), as re-plotted in Fig. 4c. The other is a group of broad-band fluctuating electromagnetic fields distributing over a wide range of extremely large values of $K_{//}$. The respective contributions to the LDOS, ρ_{SPlP} and ρ_{Fluc}, from the SPlP-mode waves and the broad-band fluctuating fields can be separately obtained by integrating $P_{EV}(K_{//}, z)$ over $1 < K_{//} < 1.0003$ and over $1.0003 < K_{//} < \infty$. It should be noted that the SPlP peak width is so small that the integrated contribution, ρ_{SPlP}, is negligibly small (even smaller than $\rho_{PG} \approx \rho_0$) in the entire range of z in Fig. 4a. Accordingly ρ_{Fluc} totally dominates the LDOS. Theory thus predicts that fluctuating electromagnetic fields of large in-plane wave numbers $K_{//}$ utterly dominate the thermal evanescent waves yielding large LDOS in the near field domain. (Large $K_{//}$ values imply also large values of $iK_\perp$ due to $K_{//}^2 + K_\perp^2 =1$.) These theoretical predictions are consistent with our experimental observations that (i) the near-field signal rapidly decreases with increasing the distance from the surface, (ii) thermal evanescent waves are those of large wave numbers, $k_{//}, ik_\perp \gg k_0$, and (iii) no signature of SPlP waves is visible.

Let us make the analysis more quantitative. We expect that the intensity of tip-scattered evanescent waves is proportional to the energy density of the evanescent waves at the probe tip position z, where we approximate the probe tip by a metal sphere of radius R with its center at a height h' above the probe apex ($z = h + h'$, inset of Fig. 2f). It follows that experimental demodulation signal is written as $I_F(h) \propto \{|\alpha_{eff}(z)|^2\rho(z) - |\alpha_{eff}(z+\Delta h)|^2\rho(z+\Delta h)\}$, where $\alpha_{eff}(z) = \alpha(1+\beta) / \{1-(\alpha\beta/16\pi z^3)\}$ with $\alpha = 4\pi R^3 (\varepsilon_W-1)/(\varepsilon_W+2)$ and $\beta = (\varepsilon-1)/(\varepsilon+1)$ is the effective polarizability of the tip.[20] Here ε_W and ε are the complex dielectric constants of the probe (W) and the sample metal,[25] and $R = 50$ nm is the tip radius. In Fig. 2f, theoretical values reproduce well the experimental rapid decay profile of I_F. The reliability of analysis is supported by the parameter value $h' = 70$ nm (obtained from the best fit) being close to $R = 50$ nm.

The disk-size dependence (Fig. 3) of the near-field signal intensity is quantitatively analyzed by assuming that $\lambda_{//}$ (or the wave number) of thermal evanescent waves on the disk of diameter D is cut off at $\lambda_{//} = D$ (or $K_{//} = \lambda_0/D$). Hence we evaluate the LDOS, $\rho(D)$, for the disk by integrating $P_{EV}(K_{//}, z, \omega)$ in Eq.(4) in the interval $\lambda_0/D < K_{//} < \infty$ instead of $1 < K_{//} < \infty$. As shown in Fig. 3, theoretical values of $\rho(D)/\rho(\infty)$ reproduce nicely the experimentally found size dependence for both Au and Al, supporting our interpretation. (This analysis does not include any adjustable parameter since $z = h + h' = 80$ nm with $h' = 70$ nm has been determined by the analysis of decay profile (Fig. 2f).)

Discussion

Our work shows that thermal motion of conduction electrons strongly couple to short-wavelength-electromagnetic fields on metal surfaces. Our work also demonstrates marked difference between the thermal excitation and the optical excitation from the viewpoint of generating SPlPs. Since SPlPs are coherent surface waves coupled with collective motion of conduction electrons, they cannot be efficiently excited by stochastic thermal motion of electrons with short correlation lengths. This situation is different from the case of optical excitation, in which monochromatic radiation is sufficiently coherent even when the radiation source is termed to be incoherent (like a black-body emitter). It is interesting to ask in which condition thermal evanescent fields on metals acquire appreciable coherence. Theory predicts a long-range coherence to occur at higher frequencies in the visible region,[26] where the surface plasmon resonance frequency is approached. Experimentally, coherent thermal radiation is hence studied for visible/near-infrared radiation thermally excited at higher temperatures (1,000 ~ 2,000 K).[27-29] The situation is different in polar dielectrics, where SPhPs in the infrared range are excited at room temperature.[30,31]

Finally we point out that our findings are largely different from what was reported earlier by de Wilde et al..[12] In their passive s-SNOM ($\lambda_0 = 10.9 \pm 0.5$ μm) measurements, Au samples are heated up to 170°C. In the work, the decay length (L_z) is mentioned to be typically as large as $L_z \approx 3$ μm for I_f and $L_z \approx 200$ nm for I_{2f}. This feature is reminiscent of the active

s-SNOM measurements,[19-23] in which I_f has a long tail due to un-filtered far-field radiation components, but is largely different from our measurements, where both $L_z \approx 40$ nm (I_f) and $L_z \approx 30$ nm (I_{2f}) are much smaller, and similar to each other.

We also note in the work that the experimentally observed fringe patterns are compared with theoretical LDOS at a height of 3 μm.[12] It should be pointed out that the absolute amplitude of theoretical LDOS is extremely small at z ≈3 μm, and in our experiments, there are no discernible near-field signals at z ≈3 μm. One should be very careful, however: Our previous work shows that, when the tip-to-surface distance exceeds ~1 μm, a signal appears both in I_f and I_{2f}, but its origin is different from the near-field evanescent waves: It is due to the background far-field radiation incident on the sample.[32] The incident radiation is partially reflected at the sample surface and scattered at the probe tip, which causes strong interference signals. Presently, we are not at the position of interpreting the experimental results of Ref.12, but we suggest that careful consideration of all these aspects is necessary to have consistent interpretation.

Methods

Ultra-highly sensitive CSIP detectors and home-made confocal microscope. The energy flux of the tip-scattered near-field thermal radiation (298K) can be roughly estimated by assuming a black-body radiation emitted through a spot size ΔX_{NF}^2 with $\Delta X_{NF} = 20 \sim 60$ nm being the near-field spatial resolution. By assuming a 10% spectral band width at $\lambda_0 = 14.5$ μm, we estimate the power in the 2π solid angle to be less than 10^{-13} Watt, which, even if reaching the detector with 100%-efficiency, is a critical level of detection when a commercial HgCdTe detector of highest sensitivity (noise equivalent power: NEP~1.0×10^{-13}W/Hz$^{1/2}$) is used. The difficulty is safely overcome by using CSIP detectors with a sensitivity (NEP~1.0×10^{-18}W/Hz$^{1/2}$) by orders of magnitude higher than that of HgAdTe detectors.[16] The detection band of CSIP is relatively narrow; $\lambda_0 = 14.5 \pm 0.7$ μm for the detector used. In order to maximize the merit of ultra-high sensitivity of the detector, we build a home-made confocal microscope (numerical aperture NA = 0.60), where the detector is housed in a cold metal can and the incidence of radiation is admitted only through a minimized pin-hole (62 μm-ϕ).[17,18] Incidence of stray radiation is whereby minimized and the theoretically optimum spatial resolution ($\Delta X_{FF} = 0.61\lambda_0/NA \approx \lambda_0 \approx 15$ μm) is achieved. The excellent far-field spatial resolution is important for realizing better fractional ratio of the near-field signal component as describe in Methods of the next paragraph.

Custom-made AFM system with independent modulation of probe tip height. Extracting near-field component out of far-field background radiation is crucially important because the far-field background radiation is much stronger. The relevant sample area for the far-field

background radiation is the focus spot of the far-field geometrical optics, ΔX_{FF}^2, which is much larger than the area, ΔX_{NF}^2, relevant to the focus spot of near-field optics. The ratio $\Delta X_{FF}^2/\Delta X_{NF}^2$ reaches an order of 10^5 when $\Delta X_{FF} \sim \lambda_0 \approx 15$ μm and $\Delta X_{NF} = 20 \sim 60$ nm are used. In actual measurements, the near-field component is typically $10^{-3} \sim 10^{-4}$ of the far-field background component.

The probe tip position is controlled in the shear-force mode of AFM, where the tip is vibrated parallel to the surface at a frequency of $\Omega \approx 32$ kHz in a small amplitude ~ 2 nm.[18] At the same time, the tip is moved up and down at a frequency $f = 10$ Hz between the heights h and $h + \Delta h$ by using an additional piezo actuator. In real practice, the bottom height h in each cycle is monitored/controlled instantaneously (with a time constant ~ 3 ms) in shear-force mode of AFM. The values of h and Δh can be chosen as independent experimental parameters in ranges of $h = 10 \sim 400$ nm and $\Delta h = 0 \sim 200$ nm. Since the atomic force range is restricted typically to $h < 40$ nm, we additionally define a reference set point at $h^* = 10$ nm for detecting the probe height to determine h and $h + \Delta h$.

Demodulation signals. The signal, $I_f(h) = I(h) - I(h + \Delta h)$ or $I_{2f}(h) = I_f(h) - I_f(h + \Delta h)$, is obtained either by taking differential signal or by demodulating the signal $I(h)$ with a Lock-in amplifier at fundamental frequency f or second harmonic frequency $2f$. A strong evidence showing that the near-field evanescent wave is rigidly extracted in our measurements is that $I_f(h)$ decays rapidly with increasing h ($L_z \approx 40$ nm) in substantially the same manner as that of $I_{2f}(h)$ ($L_z \approx 30$ nm). Furthermore, by thoroughly studying $I_f(h)$ and $I_{2f}(h)$ as a function of both h and Δh, we can confirm the consistency of our measurements in figuring out the out-of–plane profile of the near-field evanescent waves. We are thereby convinced that extraction of the near-field component is perfect both in $I_f(h)$ and $I_{2f}(h)$.

Fabrication of samples. The metal layers are patterned to a thickness of 50-80 nm on the substrates via standard optical and electron-beam lithography techniques. The metal layers are thick enough to avoid substrate-specific effects.[33]

References

1. Joulain, K., Mulet, J.-P., Marquier, F., Carminati, R. & Greffet, J.-J. Surface electromagnetic waves thermally excited: Radiative heat transfer, coherence properties and Casimir forces revisited in the near field. *Surf. Sci. Reports* **57**, 59-112 (2005).

2. C. M. HARGREAVES. Anomalous radiative transfer between closely-spaced bodies. *Phys. Lett.* **30A**, 491-492 (1969)

3. Xu, J.-B. et al., Heat transfer between two metallic surfaces at small distances. *J. Appl. Phys.* **76**, 7209-7216 (1994).

4. Kralik, T. et al. Strong near-field enhancement of radiative heat transfer between metallic surfaces. *Phys. Rev. Lett.* **109**, 224302-1/5 (2012).

5. Rousseau, E. et al. Radiative heat transfer at the nanoscale. *Nature Photon.* **3**, 514-517 (2009).

6. Shen, S. Narayanaswamy, A. & Chen, G. Surface phonon polaritons mediated energy transfer between nanoscale gaps. *Nano Lett.* **9**, 2909-2913 (2009).

7. Worbes, L. Hellmann, D. & Kittel, A. Enhanced near-field heat flow of a monolayer dielectric island. *Phys. Rev. Lett.* **110**, 134302-1/5 (2013).

8. Song, B. et al., Enhancement of near-field radiative heat transfer using polar dielectric thin films. *Nature Nanotech.* **10**, 253-258 (2015).

9. Barnes,W.L. Dereux, A. & Ebbesen, Th.W. Surface plasmon subwavelength optics. *Nature* **424,** 824-830 (2003).

10. Zia, R. & Brongersma, M. L. Surface plasmon polariton analogue to Young's double-slit experiment. *Nature Nanotech.* 2, 426-429 (2007).

11. Bitzera, A. & Walther, M. Terahertz near-field imaging of metallic subwavelength holes and hole arrays. *Appl. Phys. Lett.* **92**, 231101 (2008).

12. De Wilde, Y., et al. Thermal radiation scanning tunneling microscopy. *Nature* **444**, 740-743 (2006).

13. Joulain, K., Carminati, R., Mulet, J.-P. & Greffet, J.-J. Definition and measurement of the local density of electromagnetic states close to an interface. *Phys. Rev. B* **68**, 245405 (2003).

14. Chapuis, P.-O., Laroche, M., Volz, S. R. & Greffet, J.-J., Near-field induction heating of metallic nanoparticles due to infrared magnetic dipole contribution. *Phys. Rev. B* **77**, 125402 (2008).

15. Babuty, A. Joulain, K. Chapuis, P,-O. Greffet, J-J. & De Wilde, Y. Blackbody spectrum revisited in the near field, *Phys. Rev. Lett.* **110**, 146103-1/5 (2013).

16. Komiyama, S. Single-photon detectors in the terahertz range. *IEEE J. Select. Topics. Quantum Elect.* **17**, 54-66 (2011).

17. Kajihara, Y., Komiyama, S., Nickels, P. & Ueda, T. A passive long-wavelength infrared microscope with a highly sensitive phototransistor. *Rev. Sci. Inst.* **80**, 063702 (2009).

18. Kajihara, Y., Kosaka, K. & Komiyama, S. A sensitive near-field microscope for thermal radiation. *Rev. Sci. Inst.* **81**, 033706 (2010).

19. Knoll, B. & Keilmann, F. Near-field probing of vibrational absorption for chemical microscopy. *Nature* **399**, 134-137 (1999).

20. Knoll, B. & Keilmann, F. Enhanced dielectric contrast in scattering-type scanning near-field optical microscopy. *Opt. Commun.* **182**, 321-328 (2000).

21. Labardi, M, Patanè, S. & Allegrini, M. Artifact-free near-field optical imaging by apertureless microscopy. *Appl. Phys. Lett.* **77**, 621-623 (2000).

22. Raschke, M. B. & Lienau, C. Apertureless near-field optical microscopy: Tip-sample coupling in elastic light scattering. *Appl. Phys. Lett.* **83**, 5089-5091 (2003).

23. Keilmann, F. & Hillenbrand, R. Near-field microscopy by elastic light scattering from a tip. *Phil. Trans. R. Soc. Lond. A* **362**, 787-805 (2004).

24. Shchegrov, A. V., Joulain, K., Carminati, R. & Greffet, J.-J. Near-field spectral effects due to electromagnetic surface excitations. *Phys. Rev. Lett*, **85**, 1548-1551 (2000).

25. Ordal, M. A., Bell, R. J., Alexander, Jr, R. W., Long, L. L. & Querry, M. R. Optical properties of fourteen metals in the infrared and far infrared: Al, Co, Cu, Au, Fe, Pb, Mo, Ni, Pd, Pt, Ag, Ti, V, and W. *Appl. Opt.*, **24**, 4493-4499 (1985).

26. Carminati, R. & Greffet, J.-J. Near-field effects in spatial coherence of thermal sources. *Phys. Rev. Lett.* **82**, 1660-1663 (1999).

27. Kreite, M., Oster, J., Sambles, R., Herminghaus, S., Mittler-Neher, S. & Knoll, W. Thermally induced emission of light from a metallic diffraction grating, mediated by surface plasmons. Optics Communications **168** _1999. 117–122

28. Heinzel, A., Boerner, V., Gombert, A., Bläsi, B., Wittwer, V. & Luther, j. Radiation filters and emitters for the NIR based on periodically structured metal surfaces. J. Mod. Optics **47**, 2399-2419 (2000).

29. Laroche, M., Arnold, C., Marquier, F., Carminati, R. & Greffet, J.-J. Highly directional radiation generated by a tungsten thermal source. Opt. Lett. **30**, 2623-2625 (2005).

30. Greffet, J.-J., Carminati, R., Joulain, K., Mulet, J.-P., Mainguy, S. & Chen, Y. Coherent emission of light by thermal sources. Nature **416**, 61-64 (2002)

31. Ito, K., Matsui, T. & Iizuka, H. Thermal emission control by evanescent wave coupling between guided mode of resonant grating and surface phonon polariton on silicon carbide plate. Appl. Phys. Lett. **104**, 051127 (2014)

32. Kajihara, Y., Kosaka, K. & Komiyama, S. Thermally excited near-field radiation and far-field interference. *Opt. Express* **19**, 7695-7704 (2011).

33. Biehs, S.-A. Thermal heat radiation, near-field energy density and near-field radiative heat transfer of coated materials. *Eur. Phys. J. B* **58**, 423-431 (2007).

Author contributions

S.K. planned and led the project, designed the detectors, supported experiments and data analysis, and wrote the manuscript. Y.K. performed experiments and data analysis, and wrote the manuscript. K.K. supported experiments and data analysis. Z.A. and T.U. designed and fabricated the detectors. All authors contributed to writing the manuscript.

Additional information

Supplementary information is available in the online version of the paper. Correspondence and requests for materials should be addressed to S.K.

Competing financial interests

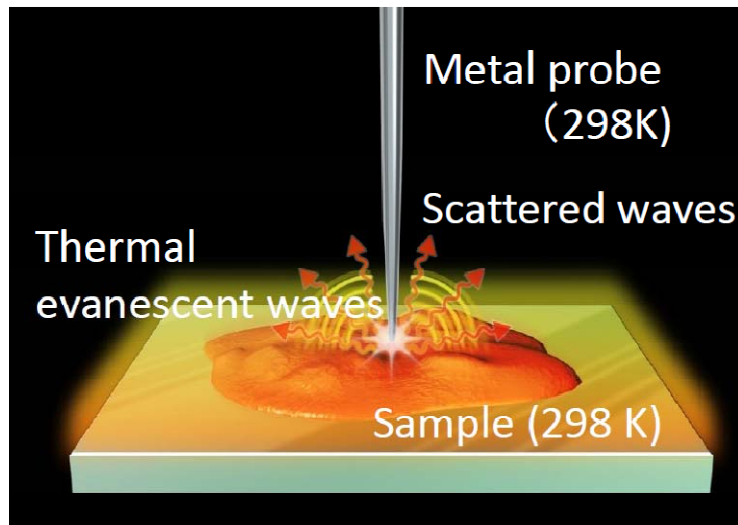The authors declare no competing financial interests.

Figure 1

Concept of passive near field microscopy.

Thermally generated evanescent wave in the close vicinity of material surface is scattered by a sharp metal probe tip (W), and the scattered waves are collected by a LWIR confocal microscope and detected with an ultra-highly sensitive CSIP detector. The detected wavelength is $\lambda_0 = 14.5 \pm 0.7$ μm ($\omega = 2\pi c/\lambda_0 \approx 1.30 \times 10^{14}$ rad/s). See text for detailed description.
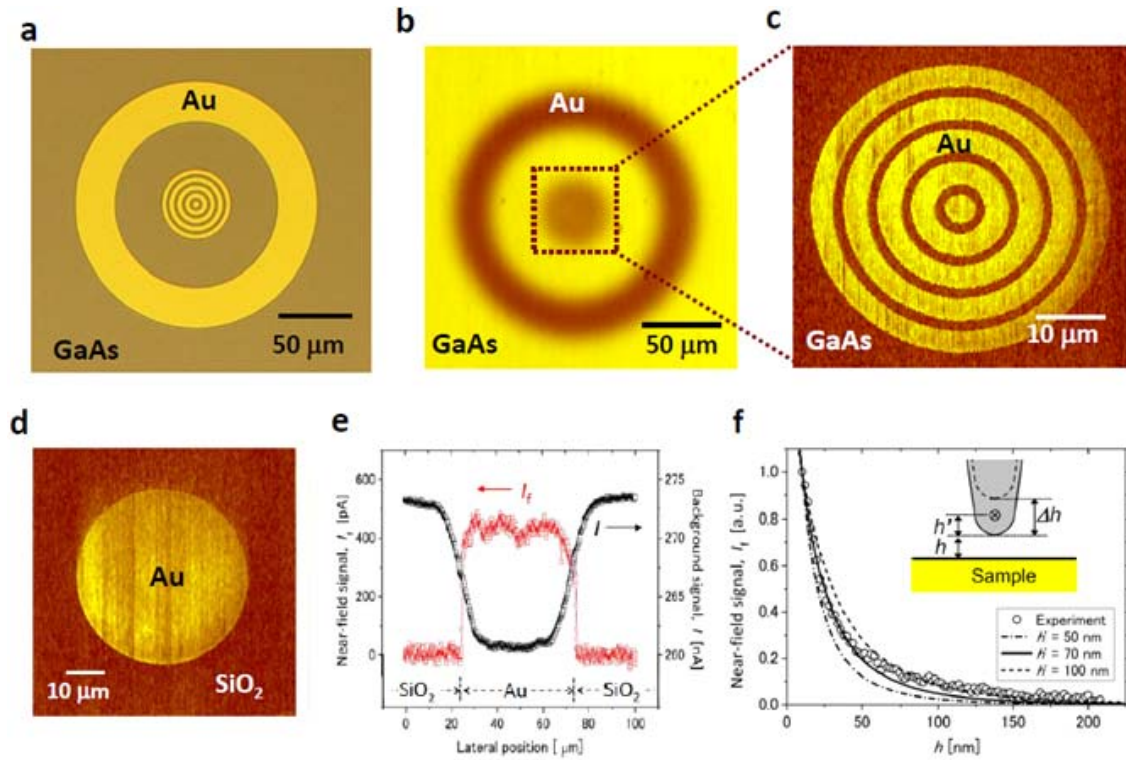
Figure 2

Near-field signals at room temperature.

a, Optical microphotograph of a sample with a pattern of 80 nm thick Au layer deposited on a GaAs substrate. The Au pattern consists of a large outer ring with smaller concentric 3 μm-wide (5 μm-pitch) rings in the central region. **b**, Far-field image (I) of the sample shown in **a**, obtained without probe modulation ($\lambda_0 = 14.5 \pm 0.7$ μm). **c**, Near-field image (I_f) obtained with $h = 10$ nm and

$\Delta h = 100$ nm . **d**, Near-field image (I_f) with $h = 10$ nm and $\Delta h = 100$ nm of a 50 μm-diameter Au disk on a SiO_2 substrate. **e**, Comparison of the far-field background signal, I, and the near-field signal, I_f ($h = 10$ nm, $\Delta h = 100$ nm), simultaneously recorded in the linear scan on the sample shown in **d**. The edge resolution at the Au/SiO_2 boundary is $\Delta X_{FF} \approx 15$ μm for the far-field signal and $\Delta X_{NF} \approx 60$ nm for the near-field signal. **f**, Near-field signal $I_f(h) = I(h) - I(h + \Delta h)$ with $h = 10$ nm and $\Delta h = 25$ nm (open circles) as a function of h on the sample shown in **d**. Three curves indicate theoretical values obtained by assuming $h' = 50$, 70 and 100 nm with $h = 10$ nm and $\Delta h = 25$ nm (see text).
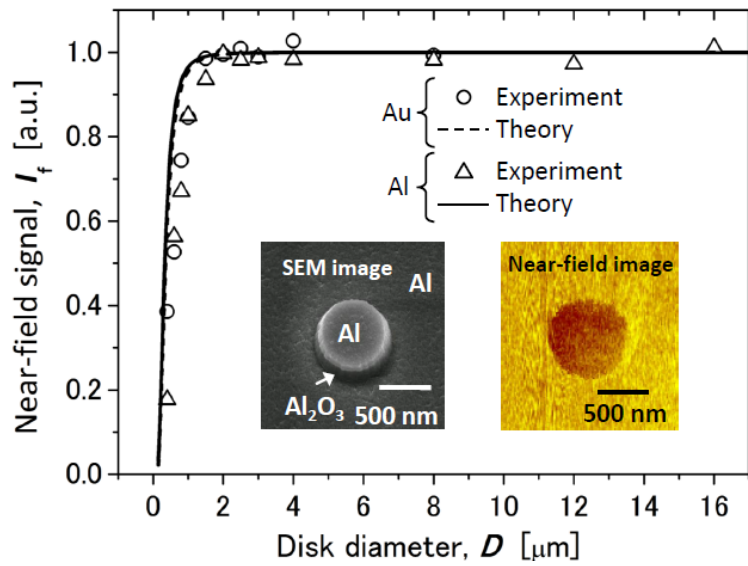
Figur 3

Sample-size dependence of near-field signals.

Near-field signal I_f ($h = 10$ nm, $\Delta h = 200$ nm) versus the diameter D of Al and Au disks, where the signal intensity is normalized by the values of large disks ($D > 8$ μm). The solid line and the broken line indicate, respectively, theoretical values of normalized LDOS, $\rho(D)/\rho(\infty)$, for disks of Al and Au with $z = 80$ nm ($h = 10$ nm, $h' = 70$ nm). The left inset is a scanning electron microscope (SEM) image of an Al disk of $D = 600$ nm. The near-field image (I_f) on the right shows that the Al disk is darker than the background Al plate.
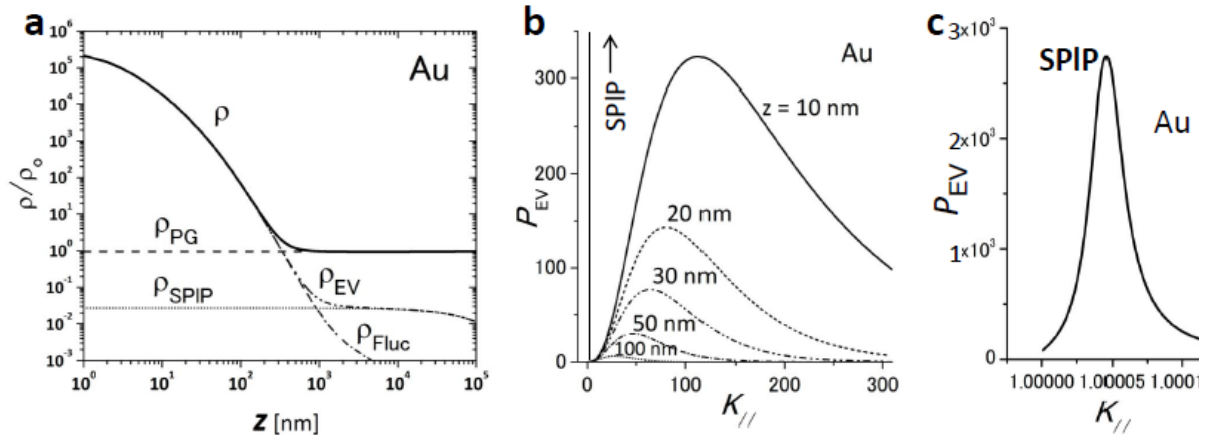
Figure 4

Electromagnetic local density of states (LDOS).

  a, LDOS versus distance z from the surface of Au at $\omega=1.30 \times 10^{14}$/s ($\lambda_0 = 14.5$ μm) . The values are normalized by the value in vacuum $\rho_0 = \omega^2/(\pi^2 c^3)$. The total LDOS, $\rho = \rho_{EV} + \rho_{PG}$, includes both of the contributions from evanescent waves, ρ_{EV} and propagating waves, ρ_{PG}, but $\rho \approx \rho_{EV}$ in the near field ($z < 200$ nm) because ρ_{EV} is much larger than ρ_{PG}. The contribution of evanescent waves, $\rho_{EV} = \rho_{SPIP} + \rho_{Fluc}$, consists of the components of SPlP-mode p-polarized surface waves, ρ_{SPIP}, and short-wavelength fluctuating electromagnetic fields, ρ_{Fluc}. The contribution from SPlP waves, ρ_{SPIP}, however, is very small (even smaller than ρ_{PG}), so that the total LDOS is utterly dominated by the fluctuating fields in the near field; viz, $\rho \approx \rho_{Fluc}$.   **b**, $P_{EV}(K_{//}, z)$ versus $K_{//} = k_{//}/k_0$. Two distinct components are distinguished. One is the sharp peak located at $K_{//} \approx 1.000045$, which is the manifestation of SPlP-mode p-polarized waves. Whereas the SPlP peak is high (a peak value reaching ca. 2600), its contribution to the LDOS, ρ_{SPIP}, is negligibly small because its integrated intensity is small. Another component, providing the dominant contribution, ρ_{Fluc}, forms a broad band of short-wavelength fluctuating fields covering a wide range of large $K_{//}$-values: The $K_{//}$-range of distribution along with the amplitude rapidly increases as z decreases. **c,** Re-plot of the SPlP-peak. Unlike the broad band of fluctuating fields, the SPlP peak (both the width and the height) is confirmed to be substantially unchanged as z varies in a range of 1nm< z <1000 nm.